RESEARCH ARTICLE

CrossMark

Solar light-driven photocatalysis using mixed-phase bismuth ferrite (BiFeO$_3$/Bi$_{25}$FeO$_{40}$) nanoparticles for remediation of dye-contaminated water: kinetics and comparison with artificial UV and visible light-mediated photocatalysis

Shankramma Kalikeri[1] · Vidya Shetty Kodialbail[1]

Abstract

Mixed-phase bismuth ferrite (BFO) nanoparticles were prepared by co-precipitation method using potassium hydroxide as the precipitant. X-ray diffractogram (XRD) of the particles showed the formation of mixed-phase BFO nanoparticles containing BiFeO$_3$/Bi$_{25}$FeO$_{40}$ phases with the crystallite size of 70 nm. Scanning electron microscopy (SEM) and transmission electron microscopy (TEM) revealed the formation of quasi-spherical particles. The BFO nanoparticles were uniform sized with narrow size range and with the average hydrodynamic diameter of 76 nm. The band gap energy of 2.2 eV showed its ability to absorb light even in the visible range. Water contaminated with Acid Yellow (AY-17) and Reactive Blue (RB-19) dye was treated by photocatalysis under UV, visible, and solar light irradiation using the BFO nanoparticles. The BFO nanoparticles showed maximum photocatalytical activity under solar light as compared to UV and visible irradiations, and photocatalysis was favored under acidic pH. Complete degradation of AY-17 dyes and around 95% degradation of RB-19 could be achieved under solar light at pH 5. The kinetics of degradation followed the Langmuir–Hinshelhood kinetic model showing that the heterogeneous photocatalysis is adsorption controlled. The findings of this work prove the synthesized BFO nanoparticles as promising photocatalysts for the treatment of dye-contaminated industrial wastewater.

Introduction

The azo dyes constitute more than 50% of the total dyeing in the textile industry and are also widely used in the printing, tannery, paper manufacture, and food and photography industries. These dyes are discharged in industrial effluents and thus cause environmental pollution. Azo dyes have a serious environmental impact, because their precursors and degradation products (such as aromatic amines) are highly carcinogenic. Azo dyes have been reported to be non-biodegradable under

aerobic conditions (O'neill et al. 2000; Basibuyuk and Forster 1997). They affect the ecosystem of streams, by either getting adsorbed or trapped in bioflocs. These dyestuffs affect the chemical oxygen demand, biochemical oxygen demand, toxicity, odor, and color of wastewater (Vinu and Madras 2012). Thus, the dye containing wastewater from industries must be treated before they are discharged into the water bodies. Government legislations on discharge standards in many countries have become increasingly stringent in order to protect the environment and to ensure sustainable growth. Though removal of color from the wastewater is the first concern, the degradation of dyes to eliminate or reduce the toxicity has always been considered as the favorable option.

Dyes can be removed from wastewater by precipitation (chemical coagulation, flocculation) (Lin and Chen 1997), adsorption (Pala and Tokat 2002), ozonation (Garc'ıa-Monta˜no et al. 2008), membrane processes such as ultrafiltration or reverse osmosis (Ghayeni et al. 1998), electrochemical processes (Naumczyk et al. 1996), and biological

✉ Vidya Shetty Kodialbail
vidyaks68@yahoo.com; vidyaks95@gmail.com;
vidyaks95@nitk.edu.in

[1] Department of Chemical Engineering, National Institute of Technology Karnataka, Surathkal, Srinivasnagar Post, Mangalore, Karnataka 575025, India

 Springer

treatment (Pala and Tokat 2002). All these techniques are versatile and useful, but they either produce secondary waste products or are uneconomical and energy intensive, and some of them may not lead to mineralization of the dyes. Photocatalysis is gaining interest among the researchers owing to its potential in mineralization of the dyes (Khanna and Shetty 2013; Soltani and Entezari 2013; Nezamzadeh-Ejhieh et al. 2013; Khanna and Shetty 2014; Chen et al. 2015). TiO$_2$ is the focus of numerous studies owing to its attractive characteristics as photocatalyst in the treatment of dye-contaminated water (Konecoglu et al. 2015; Garg et al. 2016; Markad et al. 2017; Borges et al. 2016). Unfortunately, its poor photocatalytic activity under visible or solar irradiation (Xia and Yin 2013; Khanna and Shetty 2013; Khanna and Shetty 2014; Ramírez-Aparicio et al. 2016) along with its susceptibility to fast recombination of photogenerated electron–hole pairs (Chatterjee et al. 2008; Wang et al. 2011a) limits its application. Solar light active photocatalysts are in demand, as these catalysts can be used in regions of intense solar irradiation and natural sunlight can be exploited for water treatment, thus reducing the demand for other energy sources which depend on the fuel sources that leave carbon footprints and cause the environmental impact.

In recent years, the multiferroic nanoparticles have attracted a great deal of attention as photocatalysts (Wang et al. 2009). Perovskite-type bismuth ferrite (BFO) which is a multiferroic material (Fischer et al. 1980; Dhanalakshmi et al. 2016) is synthesized by various methods such as hydrothermal method (Li et al. 2009), sol–gel method (Soltani and Entezari 2013; Wang et al. 2011b), co-precipitation method (Liu et al. 2010; Xie et al. 2014; Muneeswaran et al.2013) and ultrasonication method (Soltani and Entezar 2013). BFO nanoparticles synthesized by ethylene glycol-assisted low-temp (140 °C) hydrothermal method have shown photocatalytic activity for degradation of Rhodamine B (RhB) under visible light illumination (Liu and Zuo 2013; Chen et al. 2015). The weak magnetic BFO nanoparticles synthesized by sol–gel method have shown photocatalytic activity for degradation of methyl orange (MO) dye under visible light irradiation (Gao et al. 2007). The pure BFO nanoparticles synthesized via ultrasound at low temperature were used for the degradation of methylene blue (MB) dye under sunlight irradiation (Soltani and Entezari 2013).

Very few studies on the synthesis of BFO nanoparticles through chemical co-precipitation method are reported in literature. In the co-precipitation method, the precipitation is carried out by using an alkaline precipitation agents such as ammonia solution in water (Muneeswaran et al. 2013; Xie et al. 2014) and NaOH (Liu et al. 2010; Shami et al. 2011). The BFO nanoparticles synthesized by Xie et al. (2014) and Liu et al. (2010) by precipitation method have been reported to exhibit ultraviolet photocatalytic activity in terms of

photocatalysis of methyl orange dye. There is no evidence for photocatalytic activity under visible and solar irradiation by BFO nanoparticles synthesized using chemical co-precipitation method.

In the present study, mixed-phase BFO nanoparticles have been synthesized by a simpler co-precipitation method using potassium hydroxide as a precipitant and their photocatalytic activity in terms of photocatalytic degradation of two synthetic dyes namely, Acid Yellow-17 (AY-17) and Reactive Blue-19 (RB-19) have been carried out under UV, visible, and solar light irradiation.

Experimental methodology

Materials

The AY-17, RB-19 dyes, bismuth(III) nitrate penthydrate (BiN$_3$O$_9$-5H$_2$O) (99.99%, trace metals basis), and iron(III) nitrate nonahydrate (FeN$_3$O$_9$-9H$_2$O) (99.99%, trace metal basis) were purchased from Sigma-Aldrich Chemicals Pvt. Ltd., Bangalore. Nitric acid and potassium hydroxide (KOH) were purchased from NICE Chemicals Pvt. Ltd., Kochi, India, and used as received. All the chemicals used were of analytic grade.

## Synthesis of bismuth ferrite nanoparticles (BFO)

For the synthesis of BFO, bismuth nitrate (BiN$_3$O$_9$-5H$_2$O) and iron nitrate (FeN$_3$O$_9$-9H$_2$O) in 1:1 M ratio were used. One hundred milliliters of 0.032 M bismuth nitrate and iron nitrate solutions were prepared in distilled water separately. Bismuth nitrate solution was sonicated for 15 min and then mixed with iron nitrate solution. Ten milliliters of 0.1 M nitric acid was added to the above solution. The mixture was then precipitated slowly by adding 10 mL of 12 M KOH solution. After stirring for an hour, the mixture was centrifuged at 1200 rpm for 10 min to separate the nanoparticles and washed with distilled water and ethanol. The nanoparticles were further separated by centrifugation and dried. The particles were calcined at 400 °C for duration of 2 h in a muffle furnace.

Characterization of BFO particles

The X-ray diffraction (XRD) analysis of the calcined BFO particles was carried out by using Rigaku diffractometer under Cu-Kα radiation (1.5406 Å) and shown in Fig. 1. The crystallite size was determined by using the Debye Scherrer's formula (Eq. 1).

$$D = K\lambda/\beta\cos(\theta) \qquad (1)$$

Fig. 1 X-ray diffraction pattern of BFO
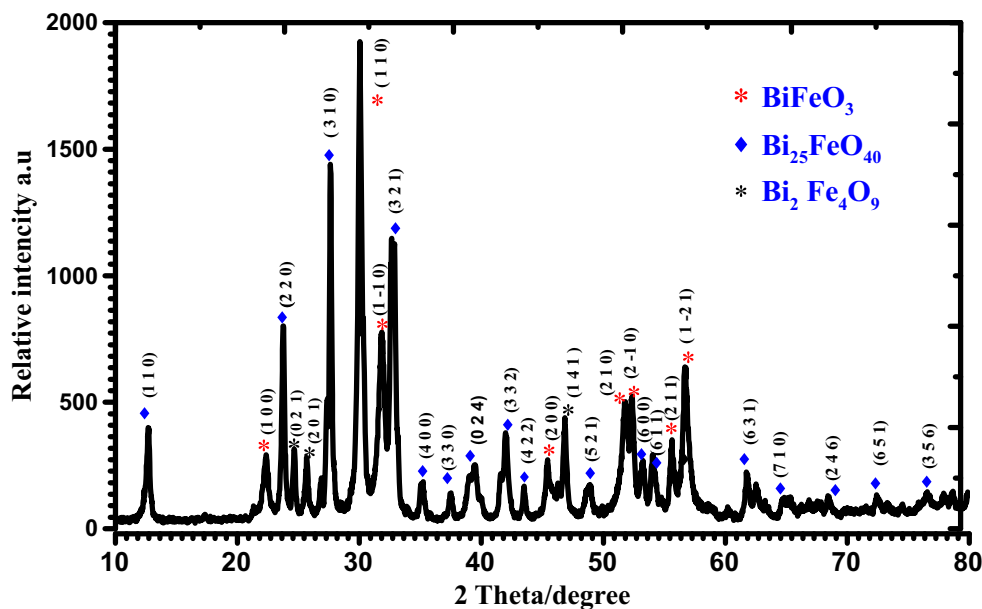
where D = crystallite size

K = 0.90 the Scherrer's constant

λ = X-ray wavelength

β = the peak width at half maximum (FWHM)

θ = the Bragg diffraction angle

The scanning electron microscopic (SEM) image was recorded by JSM-6380A operated at 20 kV. The transmission electron microscopy (TEM) was performed using a Tecnai G2T20 model with filament LaB6, and point resolution was 0.24 nm. Energy-dispersive spectrum (EDS) was also obtained using TEM. Fourier transform infrared spectroscopic (FTIR) analysis of the BFO particles was performed using Bruker Alpha FTIR spectrometer by using KBr pellets. Particle size analysis was performed on a Horiba Scientific, Nano partica, Nano particle analyzer, SZ-100. To determine the band gap energy of the synthesized catalyst, the UV-Vis spectra of the photocatalyst suspended in distilled water were obtained using Hitachi U-2000 spectrophotometer in a wavelength range of 200 to 800 nm, and the absorbance values were recorded.

Photocatalytic degradation of dyes

Photocatalysis was carried out in a 250-mL borosilicate glass beaker placed inside an aluminum chamber for UV or visible light irradiation experiments. Two irradiating lamps were mounted on the side walls of the chamber, and the beaker was placed at the center and equidistant from both the lamps. UV photocatalysis was carried out under irradiation by two 18 W UV tube lights (wavelength, k = 365 nm, Philips), and visible light experiments were carried out with irradiation using two 18 W tube lights (Polite gold, Mysore Lamps, India). Heated air in the chamber was driven out through an

exhaust fan fitted on top of the chamber, so that a constant temperature was maintained inside the reactor. The reactor contents were magnetically stirred. Solar photocatalysis experiments were performed in an open terrace during the month of March at 10:00 a.m. to 1:00 p.m., in the similar reactor setup without aluminum enclosure.

Photocatalytic degradation of two dyes, AY-17 and RB-19, with BFO nanoparticles as photocatalyst were tested. Batch experiments for the photocatalytic degradation of dyes were carried out using the fabricated BFO nanoparticles as photocatalysts under UV, visible, and solar light irradiation with 100 mL of 10 mg/L dye solution. The initial pH of the reaction mixture was adjusted to the required values using either 0.01 N NaOH or 0.01 N H_2SO_4 solutions. The experiments were conducted with a catalyst loading of 0.1 g/L under constant stirring conditions. UV and visible light-mediated photocatalysis was carried out with provision of air flow of 2 LPM to ensure the supply of oxygen as the oxidant. Additional air supply was not provided for solar light experiments, as open air and stirred conditions ensured proper supply of oxygen. Water samples were withdrawn at regular intervals of time from the reaction mixture and then centrifuged at 12,000 RPM for 10 min to separate the catalyst prior to analysis. The absorbance of the solution was measured at 418 nm for analysis of AY-17 dye concentration and 609 nm for RB-19 dye concentration using a UV-visible spectrophotometer (model: U-2000, Hitachi). The percentage of degradation of dye was estimated using Eq. 2.

$$\text{Degradation } (\%) = \frac{(C_i - C)}{Ci} \times 100 \qquad (2)$$

where C_i and C are the initial concentration and the concentrations of dye at a particular time in the reactor, respectively. Experiments were conducted for each of the dyes under UV, visible, and solar light irradiation. The effect of initial pH was studied by performing the experiments with initial pH of 5, 7, and 9.

Results and discussion

Characterization of BFO particles

Figure 1 shows the XRD pattern of BFO particles synthesized by co-precipitation method. Peaks are exhibited at $2\theta = 22.4°$, $31.8°$, $32.07°$, $46°$, $51.5°$, $51.8°$, $56.46°$, and $57.16°$ corresponding to BFO of different crystalline plane (1 0 0), (1 1 0), (1 −1 0), (2 0 0), (2 1 0), (2 −1 2), (2 1 1), and (1 −2 1), respectively, which confirmed the presence of perovskite $BiFeO_3$ (JCPDS-ICDD PDF Reference No. -01-072-2035) with rhombohedral crystal system. The peaks at $2\theta = 12.2$, $24.7°$, $27.6°$, $32.8°$, $35.2°$, $37.5°$, $39.5°$, $42°$, $43.5°$, $48.9°$, $54.0°$, $61.74°$, $64.7°$, 68.4, 73.1, and 78.6 corresponding the crystalline planes (1 1 0), (2 2 0), (3 1 0), (3 2 1), (4 0 0), (3 3 0), (0 2 4), (3 3 2), (4 2 2), (5 2 1), (6 0 0), (6 3 1), (6 3 1), (7 1 0), (2 4 6), (6 5 1), and (3 5 6) indicate the presence of $Bi_{25}FeO_{40}$ (JCPDS-ICDD PDF Reference No. -01-078-1543) with cubic crystal system. The peaks at $2\theta = 25.8$, $26.8°$, and $47°$ correspond to $Bi_2Fe_4O_9$ with crystalline planes (0 2 1), (2 0 1), and (1 4 1) (JCPDS-ICDD PDF Reference No. -00-025-0090) with orthorhombic crystal system. XRD analysis shows the formation of mixed-phase BFO containing $BiFeO_3$, $Bi_{25}FeO_{40}$, the oxygen-deficient impurity phase, and traces of $Bi_2Fe_4O_9$ which is the Bi-deficient or Fe-rich impurity phase. The formation of $Bi_2Fe_4O_9$ and $Bi_{25}FeO_{40}$ as impurities might be ascribed to the decomposition of $BiFeO_3$ during the slow heating process. The involved chemical reactions can be expressed as follows (Wang et al. 2011b):

$$4BiFeO_3 \longrightarrow Bi_2Fe_4O_9 + Bi_2O_3 \qquad (3)$$

$$BiFeO_3 + 12Bi_2O_3 + 0:5O_2 \longrightarrow Bi_{25}FeO_{40} \qquad (4)$$
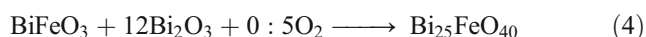
Gao et al. (2014) have reported the visible light activity of pure $BiFeO_3$ synthesized by sol–gel method with ethylene glycol as the solvent in degradation of methyl orange dye. Xian et al. (2011) have synthesized pure $BiFeO_3$ by thermal decomposition process of xerogel and have reported its UV and visible light photocatalytic activity for the degradation of methyl orange dye. Zhang et al. (2016) have shown that the oxygen-deficient phase of bismuth ferrite, $Bi_{25}FeO_{40}$, also shows excellent visible light-mediated photocatalytic activity. Zhang et al. (2015) have successfully synthesized $Bi_{25}FeO_{40}$ tetrahedrons through a facile, mild, and rapid hydrothermal route and have reported visible light photocatalytic activity for the degradation of RhB.

Ruan and Zhang (2009) have reported the visible light photocatalytic activity of $Bi_2Fe_4O_9$ nanosheets in dye degradation. The nanoparticles synthesized in the present study contain mixed-phase BFO majorly containing $Bi_{25}FeO_{40}$ and $BiFeO_3$ as well as traces of $Bi_2Fe_4O_9$, all of which have been reported to show excellent visible light photocatalytic activity. Many oxides have different polymorphic crystal structures which can be used for heterojunction performance because their different crystal structures at two sides of the interface may be helpful for carrier separation across the interface (Ohno et al. 2001; Fan et al. 2012; Ju et al. 2014). For example, rutile-anatase mixed-phase TiO_2 has been shown to have much higher activity than single-phase systems for water splitting (Pan et al. 2011; Ohno et al. 2001; Li and Gray 2007). Thus, it is hypothesized that the mixed-phase BFO nanoparticles synthesized in the present work may exhibit good visible light activity. According to the XRD results and Debye Scherrer's formula, the average crystallite size was found to be 70 nm. In the SEM image presented as Fig. 2a, the particles formed seem to be small, quasi-spherical, or oval shaped, with a few large aggregates. Figure 2b illustrates the EDS spectra of BFO nanoparticles, which showed the presence of O, Fe, and Bi elements. The TEM image presented in Fig. 3 also reveals the presence of quasi-spherical-shaped particles and aggregates. Figure 4 shows the size distribution of the particles as obtained by dynamic light scattering (DLS) technique (Carney et al. 2011) with deionized water as the solvent. The size distribution is in a very narrow range indicating the formation of uniform-sized particles. The average hydrodynamic diameter is shown as 76 nm.

To determine the apparent band gap energy for the mixed-phase BFO, the absorption spectrum of BFO nanoparticles was obtained using UV-Vis spectrophotometer and is shown in Fig. 5a. The cutoff wavelength was found to be 560 nm showing that these nanoparticles can absorb light both in the UV and visible range. The apparent optical energy band gap of the synthesized BFO nanoparticles was calculated by using Tauc's plot shown in Fig. 5b plotted from the data of the absorption spectra. Tauc's plot of $(Ah\nu)^2$ vs $(h\nu)$ was plotted, where A is the absorbance, h is the Plank's constant, and $\nu = c/\lambda$ ($c =$ speed of light and λ is the wavelength). The presence of linear region in the Tauc's plot indicates that $BiFeO_3$ nanoparticles are direct band gap semiconductive material (Wang et al. 2010; Yang et al. 2005; Wang et al. 2011b).

The extrapolation of the linear region of the Tauc's plot intersecting the x-axis gives the value of the optical band gap, E_g. The calculated value of apparent band gap energy is 2.2 eV, which is lower than the band gap values reported

Fig. 2 **a** Scanning electron microscopic image of BFO nanoparticles. **b** Energy-dispersive X-ray spectral peaks (EDAX) of BFO nanoparticles

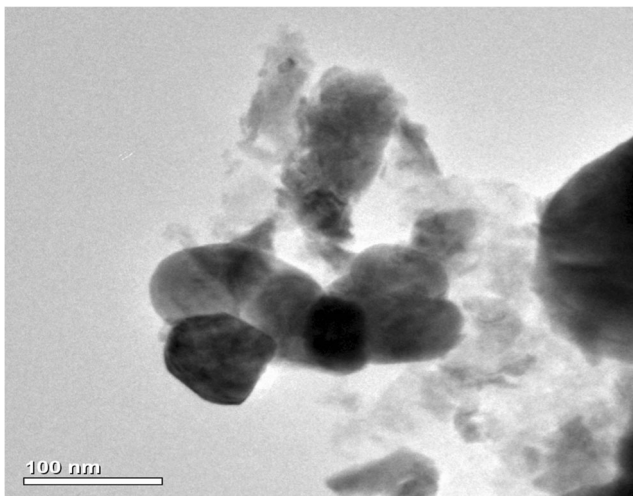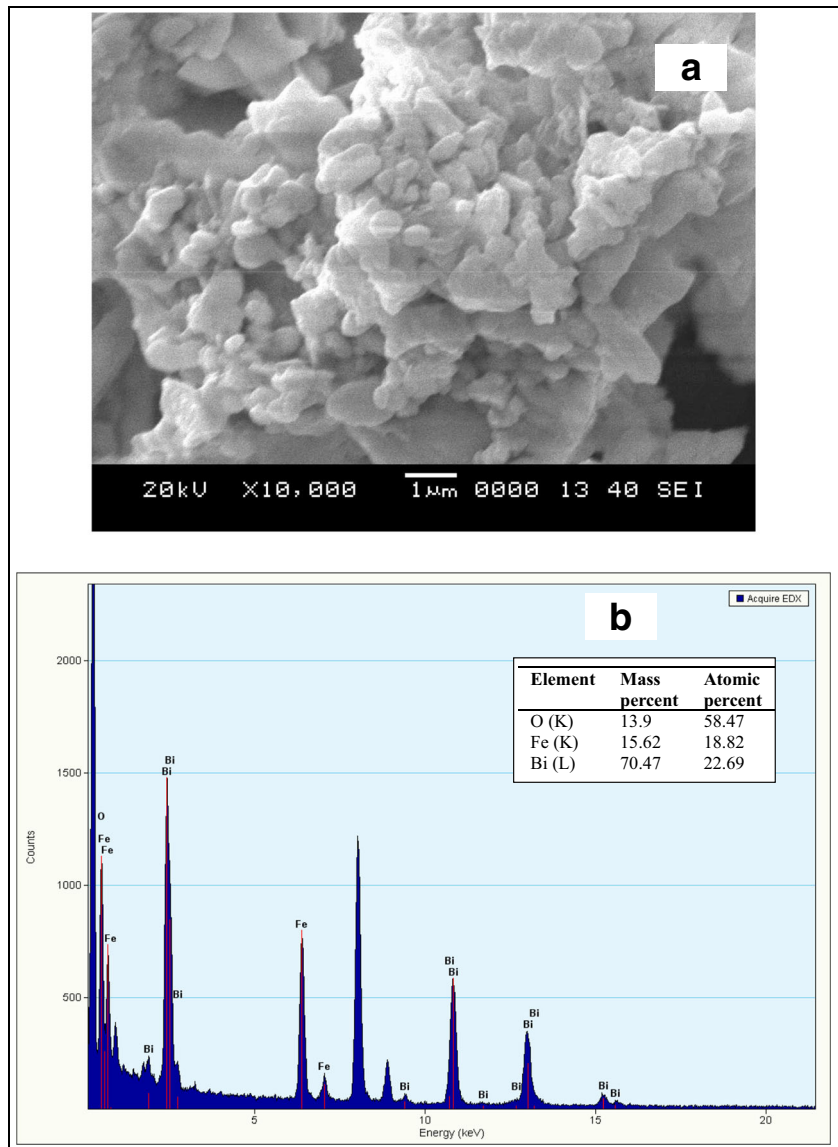| Element	Mass percent	Atomic percent
O (K)	13.9	58.47
Fe (K)	15.62	18.82
Bi (L)	70.47	22.69

Fig. 3 Transmission electron microscopic image of BFO nanoparticles

by Xie et al. (2014) and Li et al. (2009) for BFO synthesized by co-precipitation and hydrothermal method. The cutoff wavelength was calculated to be 560 nm. The cutoff wavelength indicates that BFO can absorb light even in longer wavelength visible region. The absorbance plot shows a strong transition in the 560 nm which corresponds to electronic transitions involving charge transfer from valence band O 2p states to conduction band Fe 3d states (Hauser et al. 2008). Though the pure phase $BiFeO_3$ has the band gap energy value of around ~2.3 eV (Mocherla et al. 2013) and pure phase $Bi_{25}FeO_{40}$ has the band gap energy value of ~1.8 eV (Wang et al. 2017), the estimated apparent band gap of mixed-phase BFO synthesized in the present study is lesser than the band gap of $BiFeO_3$ and greater than the band gap of $Bi_{25}FeO_{40}$. The band gap energy value of 2.2 eV for the BFO nanoparticles synthesized in the present study implied that the light with λ less

Fig. 4 Size distribution of BFO nanoparticle measured by the DLS technique
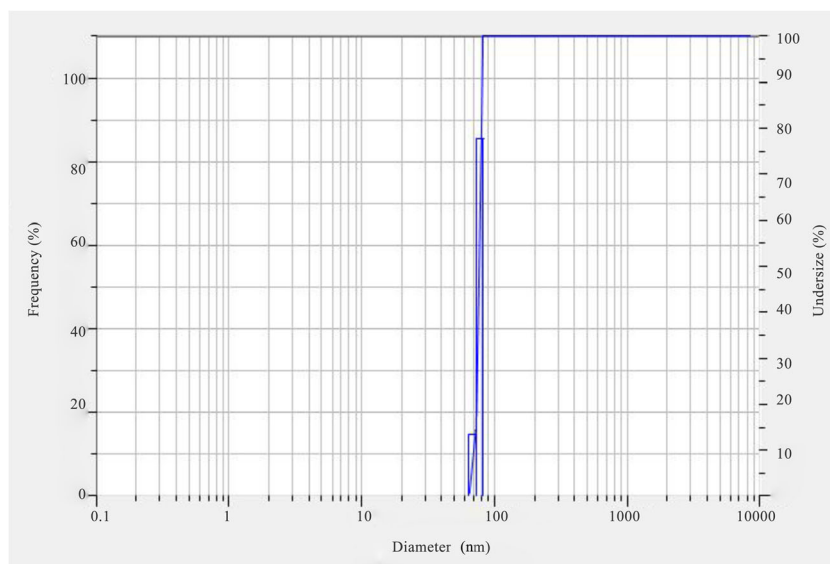

than 560 nm could be absorbed by electrons to jump to the conduction band (CB) from the valence band (VB) in BFO. The band gap value of mixed-phase BFO is lesser than that of pure phase $BiFeO_3$ nanoparticles. The existence of defect-induced energy levels between the conduction and valence bands may lower the apparent band gap value for the semiconductors (Mocherla et al. 2013). The energy levels are modified by the presence of non-uniform microstrain in the particles, and they influence the absorption band edge (Smith et al. 2009). In general, the microstrain in nanocrystallites is caused by several factors like non-uniform lattice distortions, dislocations, antiphase domain boundaries, and grain surface relaxation. In $BiFeO_3$, the most common defects such as oxygen vacancies (Hauser et al. 2008) or the unsaturated bonds on the surface of the nanoparticles, which create deep and shallow levels within the band gap, are major contributors to the microstrain (Sattler 2002). In stoichiometric $BiFeO_3$, the band gap is between the O 2p and Fe 3d levels. The oxygen vacancies lower the adjacent Fe 3d levels, resulting in sub-band gap defect states (Hauser et al. 2008). According to Hauser et al. (2008), the theoretical calculations suggest that defect states due to oxygen vacancies lead to transitions at ~ 0.3 eV below the band gap. First-principle studies conducted by Ju and Cai (2009), on the optical properties,

have shown that the absorption edge gets smoother and shifts to lower energy with increasing oxygen vacancy concentration. Further, in mixed-phase BFO, charge transfer occurs between the phases, creating hole centers at $BiFeO_3$ and electron centers at $Bi_{25}FeO_{40}$, thus reducing charge recombination rates. Lower apparent band gap values of the synthesized BFO nanoparticles show them to be promising and highly active visible light photocatalysts.

In Fig. 6, the FTIR spectrum is shown. Three intense peaks at 430, 456, and 501 cm^{-1} are due to stretching and bending vibrations of Fe–O bond, respectively, and are fundamental absorptions of FeO_6 octahedral in perovskite. The formation of perovskite structure of BFO in the present work can be confirmed by the presence of metal oxide band at 400–600 cm^{-1} (Ke et al. 2011). The peaks around 1333 and 1031 cm^{-1} were due to the presence of nitrate ions (Zalesskii et al. 2003; Muneeswaran et al. 2013). The strong and broad peak at 3411.98 indicates O–H stretching vibration due to intermolecular H bonds. The peak at 1628 cm^{-1} corresponds to stretching and bending vibration of water molecules (Cao et al. 2016). The peaks around 1476 cm^{-1} may be attributed to C–H bending (Simões et al. 2008; Gabbasova et al. 1991) owing to the presence of traces of ethanol on the surface which was used for washing the nanoparticles.

Fig. 5 **a** UV-visible spectra of BFO nanoparticles. **b** Tauc plot for band gap of BFO nanoparticles
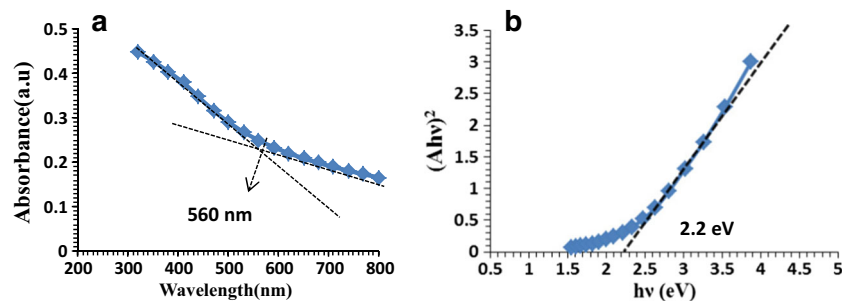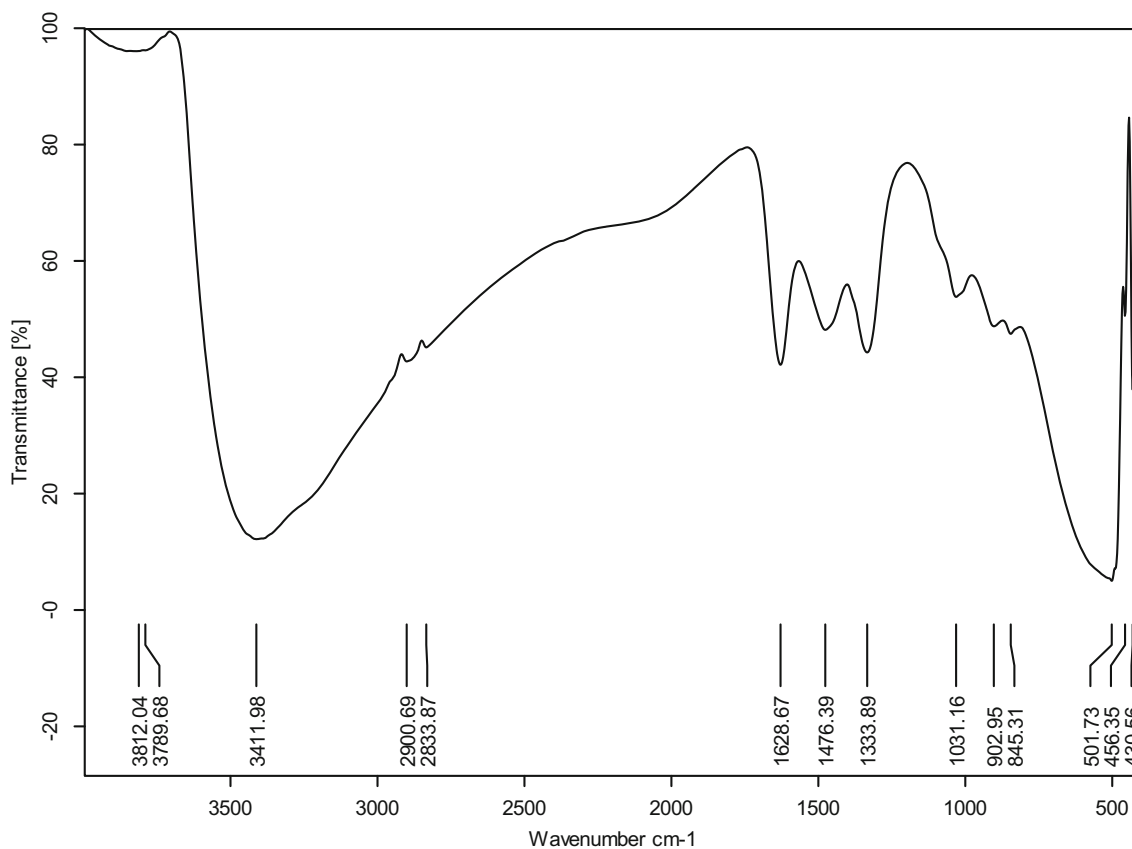
Fig. 6 FTIR spectra of BFO nanoparticle

Determination of photocatalytic activity of BFO nanoparticles under UV, visible, and solar light irradiation

The efficiency of BFO nanoparticles as a photocatalyst in degradation of AY-17 and RB-19 dyes under UV, visible, and solar light irradiation was studied with initial concentration of dye at 10 mg/L and catalyst loading of 0.1 g/L. Figure 7a, f shows that the percentage dye removal under dark conditions in the presence of catalyst is very minimal (less than 8%) as compared to that in the presence of catalyst on irradiation with solar, UV, or visible light. Thus, the dye removal by adsorption on the catalyst is minimal. The effect of the light irradiation in the absence of catalyst is also very less, confirming a small effect of photolytic removal of the dyes by solar, UV, and visible light irradiation.

As observed in Fig. 7a, b, almost 100% degradation of Acid Yellow and Reactive Blue-19 dyes could be achieved in 135 min of irradiation time under solar light. However, under UV light around 90% degradation of AY-17 dye and 86% degradation of RB-19 dye occurred in 135 min as observed in Fig. 7c, d. Figure 7e, f shows that around 85% degradation of AY-17 dye and 84% degradation of RB-19 dye occurred in 135 min under visible light irradiation. These results indicate that BFO nanoparticles are photocatalytically active under solar, UV, and visible light irradiation. As observed from these results, the photocatalytic activity of the BFO nanoparticles under solar light is better than those under UV or visible light. However, the visible light activity is lesser than the UV light activity. The highest activity under solar light may be attributed to the fact that solar light comprises of light in both UV and visible light wavelength range and BFO nanoparticles are able to absorb light both in UV and visible light wavelength range. The high photocatalytic efficiency exhibited under solar light is due to the low band gap energy of 2.2 eV for BFO nanoparticles. As observed from the absorbance spectra in Fig. 5a, maximum absorbance is exhibited at wavelength of 300 nm and the absorbance values decreased as the wavelength increased. It shows that the maximum absorption by BFO nanoparticles occurs in UV range. The absorbance reduces with increase in wavelength, and the absorbance edge occurs at 560 nm, thus showing that the BFO nanoparticles absorb light in the wavelength range less than 560 nm. With the maximum absorption occurring at UV range, the electron hole separation and hydroxyl radical formation rates are faster under UV light, and thus, higher photocatalytic activity has been observed under UV light as compared to visible
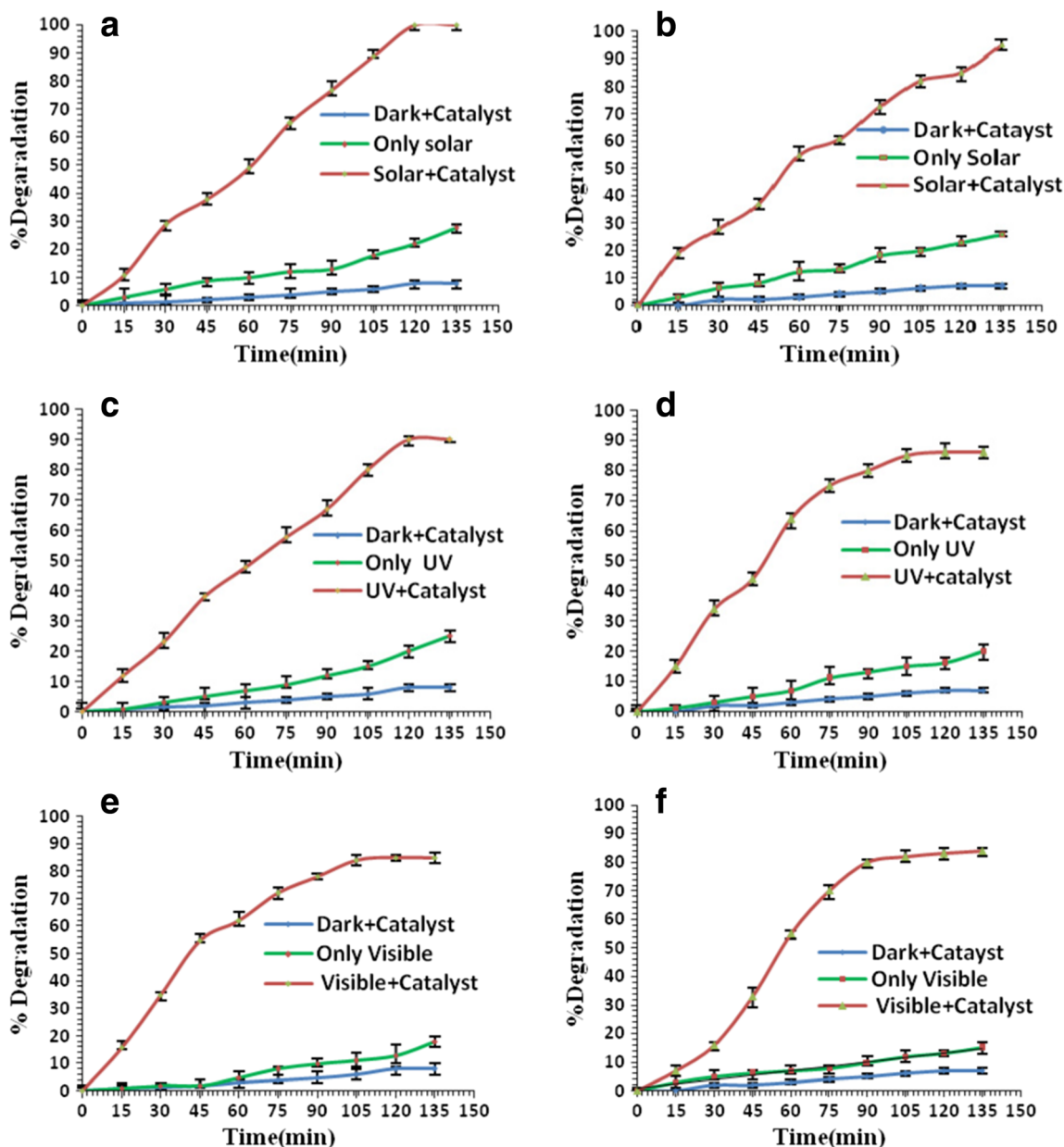
Fig. 7 Photocatalytic activity of BFO nanoparticles under **a** solar light for AY-17, **b** solar light for RB-19, **c** UV light for AY-17, **d** UV light for RB-19, **e** visible light for AY-17, and **f** visible light for RB-19

light. Under UV irradiation, light in the wavelength range less than 400 nm is absorbed, whereas under visible light irradiation, the light with wavelengths in the range of 400 to 560 nm is absorbed. As solar light contains entire spectrum of radiation, light absorption by BFO occurs at all wavelengths less than 560 nm under solar light, thus leading to maximum photon availability for excitation of the nanoparticles followed by faster separation of electron and holes, thus resulting in maximum photocatalytic activity under solar light.

The photocatalytic activity of these mixed-phase BFO nanoparticles is better than the pure phase BFO reported in literature as presented in Table 1. In the present study, the mixed-phase BFO nanoparticles synthesized by co-precipitation method using KOH as the precipitant has shown enhanced photocatalytic activity under solar irradiation as well as under artificial visible and UV light irradiation as compared to those reported in literature, with complete degradation in around 135 min with catalyst loading of 0.1 g/L under solar light. The photocatalysis has utilized only oxygen from the air as the oxidant with no addition of any other oxidants. This proves that the mixed-phase BFO has enhanced photocatalytic activity. These results show that the mixed-phase BFO nanoparticles are very active

Table 1 Degradation of dyes by using BFO nanoparticles

Catalyst	Dye	Light source (irradiation time)	Percentage degradation	Reference
2.5 g/L pure BFO	10 mg/L methyl orange	UV (6 h) Visible (14 h)	71% 39%	Xian et al. (2011)
0.03 g/L pure BFO	5 mg/L methyl orange	Visible (450 min)	Complete degradation	Gao et al. (2014)
BFO with inverse opal structure	10 mg/L Rhodamine B	UV (2 h)	7 to 8%	Tan et al. (2015)
0.1 g/L of hydrothermally grown BFO With O_2 and H_2O_2 as the oxidant	3.9 mg/L methyl violet dye	Solar (2 h)	40% (O_2 as oxidant) Complete degradation (H_2O_2 as oxidant)	Dhanalakshmi et al. (2016)
0.1 g/L with mixed-phase BFO nanoparticles	10 mg/L AY-17	UV (135 min) Visible (135 min) Solar (135 min)	90% 85% Complete degradation	Present study
0.1 g/L with mixed-phase BFO nanoparticles	10 mg/L RB-19	UV (135 min) Visible (135 min) Solar (135 min)	86% 84% Complete degradation	Present study

photocatalysts and can be used for wastewater treatment to degrade the dyes under solar light in regions where solar light is abundantly available. However, artificial UV or visible light irradiation can be adopted for the photocatalytic water treatment when solar light is not available.

The photocatalytic reaction mechanism is represented in the schematic illustration shown in Fig. 8. When the energy of light in terms of photon is equal to or greater than the band gap of BFO, the electrons receive energy and transfer of electrons takes place from the VB to the CB which result in the creation of a hole (h+) in the VB and an electron (e⁻) in the CB. In the mixed-phase BFO, $BiFeO_3$ has the band gap energy value of around ~2.3 eV (Mocherla et al. 2013) and $Bi_{25}FeO_{40}$ has the band gap energy value of ~1.8 eV (Wang et al. 2017). The electrons from the conduction band of $BiFeO_3$ get transferred to the conduction band of

$Bi_{25}FeO_{40}$, and thus, the conduction band of $Bi_{25}FeO_{40}$ acts as electron centre. The holes in the valence band of $Bi_{25}FeO_{40}$ transfer to the valence band of $BiFeO_3$ and thus forming hole center in $BiFeO_3$. Thus, electron hole recombination rate reduces, leading to superior photocatalytic activity of mixed-phase BFO. The apparent band gap energy of the mixed-phase BFO is also lower than $BiFeO_3$, thus making it a better visible light active photocatalyst. The holes react with water and generate hydroxyl radicals, which can oxidize the organic pollutants. The electron in the conduction band of $Bi_{25}FeO_{40}$ reacts with oxygen on the catalyst surface in the reduction process and produces oxide radicals. These oxide radicals reduce the organic pollutants. The oxide radicals may further lead to the formation of hydroxyl radicals. These oxidation and reduction processes lead to degradation of the organic pollutants under solar,
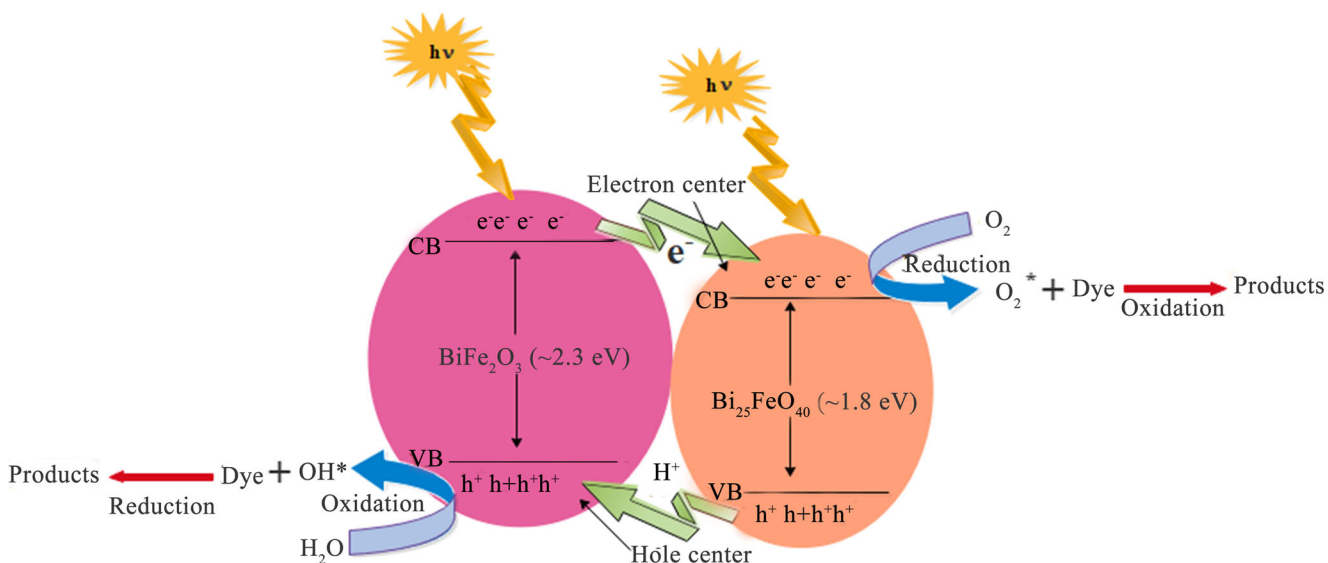

Fig. 8 Proposed mechanism for photodegradation of dyes by fabricated BFO nanoparticles under UV, visible, and Solar light
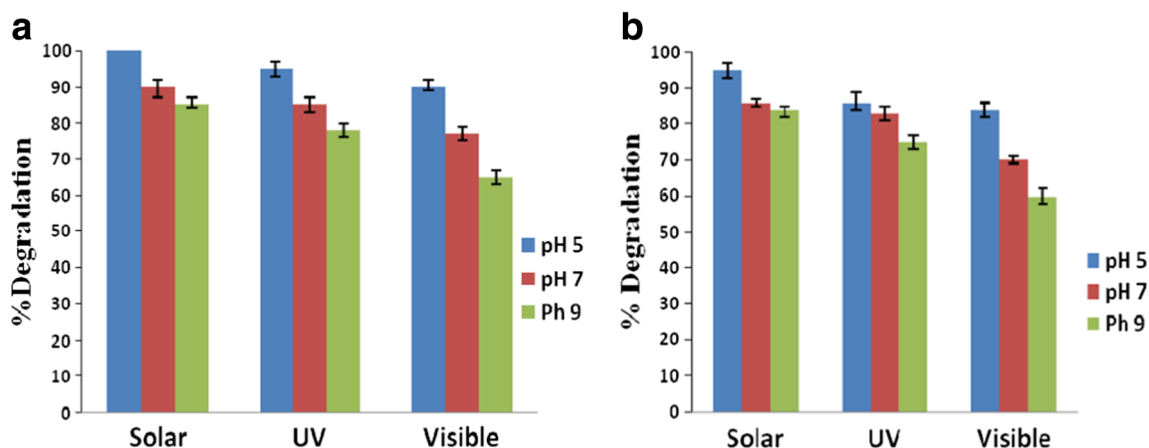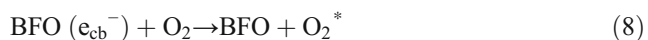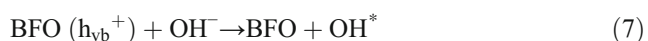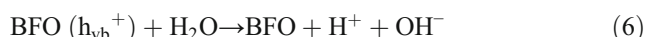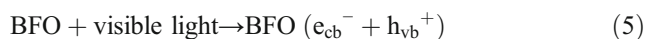
Fig. 9 Percentage degradation of **a** AY-17 and **b** RB-19 dyes at different pH under solar, UV, and visible light irradiation

UV, or visible light irradiation. The scheme of reaction series occurring during photocatalytic process is presented below (Khanna and Shetty 2013).

$$BFO + visible\ light \rightarrow BFO\ (e_{cb}^- + h_{vb}^+) \quad (5)$$

$$BFO\ (h_{vb}^+) + H_2O \rightarrow BFO + H^+ + OH^- \quad (6)$$

$$BFO\ (h_{vb}^+) + OH^- \rightarrow BFO + OH^* \quad (7)$$

$$BFO\ (e_{cb}^-) + O_2 \rightarrow BFO + O_2^* \quad (8)$$

$$Dye + OH^* \rightarrow products \quad (9)$$

$$Dye + O_2^* \rightarrow products \quad (10)$$

Effect of pH on the photocatalytic degradation of AY-17 and RB-19 dyes under solar, UV, and visible light irradiation

pH of the solution is one of the prominent factors which affect photocatalysis (Barakat et al. 2005). Thus, the effect of pH on degradation of AY-17 and RB-19 dyes using BFO nanoparticles under UV, visible, and solar irradiation was studied. The experiments were conducted with initial dye concentration of 10 mg/L and with 0.1 g/L of BFO loading. Figure 8 presents the percentage degradation of AY-17 and RB-19 dyes obtained after an irradiation period of 135 min at different initial pH conditions of 5, 7, and 9. As shown in Fig. 9, the percentage degradation of the dye decreased when the initial pH was increased from acidic to neutral and then to alkaline conditions. The maximum degradation of both the dyes occur at pH 5 under solar, UV, and visible light irradiation. Acidic pH is found favorable. The surface charge of BFO nanoparticles changes with change of solution pH. According to Soltani and Entezari (2013), positive holes predominantly act as the major oxidation species at acidic pH, whereas hydroxyl radicals act as the predominant species in neutral or higher pH. AY-17 and RB-19 are the anionic dyes (Ashraf et al. 2013; Hadjltaief et al. 2014). In acidic solutions, the surface of the photocatalyst may have positive charge due to the increase in the H^+ ions in the solution, which leads to strong electrostatic attraction between the positive charge of the surface and anionic dye molecules and thus increases the adsorption rate. In high pH levels, hydroxyl ions compete with the dye anions for the adsorption sites (Brunauer et al. 1938; Alkan et al. 2004). Higher adsorption at lower pH values facilitate higher rate of photocatalysis at acidic pH.
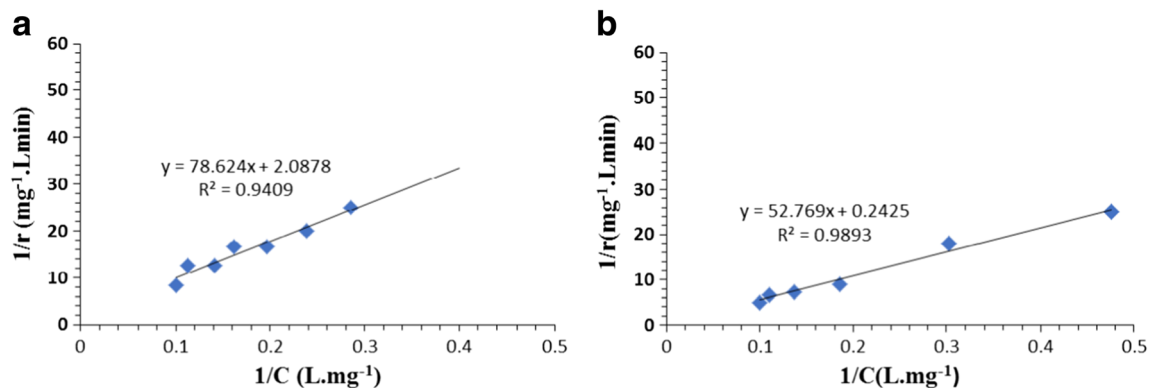

Fig. 10 Plot for pseudo-first-order kinetics of degradation of **a** AY-17 and **b** RB-19 dyes under solar light at conditions: pH = 5, catalyst used = 0.1 g/L

Table 2 Values of K_{obs} and K_R for degradation of kinetics for AY-17 and RB-19 under solar light

Color (dye)	AY-17	RB-19
K_{obs} (mM/min)	8.7×10^{-4}	6.5×10^{-3}
K_R (mM^{-1})	14.61	2.878

Kinetics of degradation of AY and RB dyes under UV, visible, and solar irradiation

The studies presented in earlier sections showed that the photocatalytic activity of BFO is the maximum under solar irradiation and at pH 5. Thus, the kinetics of photocatalysis of AY-17 and RB-19 under solar light with initial pH of 5 was evaluated. Studies on kinetics of degradation help in the prediction of rate equation. The Langmuir–Hinshelwood (L–H) model presented as Eq. (11) (Matthews 1987) is generally used to describe the solid–liquid reaction successfully.

$$r = K_{obs} K_R \ C/(1 + K_R \ C) \tag{11}$$

where r is the reaction rate, C is the concentration of the dye (color) in millimolar, K_{obs} is the constant, related to adsorption, and K_R is the reaction rate constant. Modified form of L–H model is given by Eq. (12)

$$\frac{1}{r} = \frac{1}{K_{obs} \ K_R C} + \frac{1}{K_{obs}} \tag{12}$$

The rate of degradation at different concentrations was determined by drawing tangents at different interval of time, on plots of dye concentration vs. time data obtained by batch experiments. $1/r$ vs. $1/C$ was plotted, and values for the kinetic parameters were estimated from the slope and intercept. The applicability of L–H equation for the degradation of both AY-17 and RB-19 dyes has been confirmed by the linear nature of the plots as shown in Fig. 10.

The R^2 values indicated in the plots show the goodness of fit. Table 2 presents the values of K_{obs} and K_R of the kinetic model for the degradation of both the dyes. Applicability of L–H kinetic equation shows that the photocatalysis of both the dyes by BFO is an adsorption-controlled process.

Conclusions

In the present study, nanocrystalline mixed-phase BFO (BiFeO$_3$/Bi$_{25}$FeO$_{40}$) particles of average particle size of 76 nm and band gap energy of 2.2 eV were synthesized by co-precipitation method using KOH. The BFO nanoparticles exhibited better photocatalytic activity in terms of degradation of two dyes, AY-17 and RB-19, under solar light irradiation as compared to that under UV or visible light irradiation. Acidic pH was found to be favorable for degradation of both the dyes under UV, visible, and solar irradiation. Around complete degradation of AY-17 dye and 95% degradation of RB-19 could be achieved in 135 min of irradiation at initial pH of 5 by solar photocatalysis. The kinetics of degradation of both the dyes under solar light followed Langmuir–Hinshelwood kinetic equation showing that photocatalysis is adsorption controlled. The present work proves that the mixed-phase BFO nanoparticles synthesized by co-precipitation method using KOH are the promising photocatalysts for treatment of dye containing effluents from industries, and they can be used for solar photocatalysis in regions of abundant sunlight for wastewater treatment by photocatalysis. Its efficacy under UV and visible light irradiation implies that it can also be used under artificial irradiation with UV or visible light during periods when solar light is not available.

References

Alkan M, Demirbaş Ö, Celikcapa S, Doğan M (2004) Sorption of acid red 57 from aqueous solution onto sepiolite. J Haz Mat 116(1-2):135–145. https://doi.org/10.1016/j.jhazmat.2004.08.003

Ashraf MA, Hussain M, Mahmood K, Wajid A, Yusof M, Alias Y, Yusoff I (2013) Removal of acid yellow-17 dye from aqueous solution using eco-friendly biosorbent. Des Water Treat 51(22-24):4530–4545. https://doi.org/10.1080/19443994.2012.747187

Barakat MA, Schaeffer H, Hayes G, Ismat-Shah S (2005) Photocatalytic degradation of 2-chlorophenol by Co-doped TiO$_2$ nanoparticles. App Cat B: Environ 57(1):23–30. https://doi.org/10.1016/j.apcatb.2004.10.001

Basibuyuk M, Forster CF (1997) The use of sequential anaerobic/aerobic processes for the bio treatment of a simulated dyeing wastewater. Environ tech 18(8):843–848. https://doi.org/10.1080/09593330.1997.9618562

Borges ME, Sierra M, Cuevas E, García RD, Esparza P (2016) Photocatalysis with solar energy: sunlight-responsive photocatalyst based on TiO$_2$ loaded on a natural material for wastewater treatment. Sol Energy 135:527–535. https://doi.org/10.1016/j.solener.2016.06.022

Brunauer S, Emmett PH, Teller E (1938) Adsorption of gases in multi molecular layers. J Ameri chem soc 60(2):309–319. https://doi.org/10.1021/ja01269a023

Cao W, Chen Z, Gao T, Zhou D, Leng X, Niu F, Huang Y (2016) Rapid synthesis of single-phase bismuth ferrite by microwave-assisted hydrothermal method. Mater Chem Phys 175:1–5. https://doi.org/10.1016/j.matchemphys.2016.02.067

Carney RP, Kim JY, Qian H, Jin R, Mehenni H, Stellacci F, Bakr OM (2011) Determination of nanoparticle size distribution together with density or molecular weight by 2D analytical ultracentrifugation. Nature comm 2:335. https://doi.org/10.1038/ncomms1338

Chatterjee D, Patnam VR, Sikdar A, Joshi P, Misra R, Rao NN (2008) Kinetics of the decoloration of reactive dyes over visible light-irradiated TiO₂ semiconductor photocatalyst. J Hazar Mat 156(1-3):435–441. https://doi.org/10.1016/j.jhazmat.2007.12.038

Chen Z, Jin W, Lu Z, Hu C (2015) Ferromagnetic and photocatalytic properties of pure BiFeO₃ powders synthesized by ethylene glycol assisted hydrothermal method. J Mat Sci: Mat Elec 26:1077–1086

Dhanalakshmi R, Muneeswaran M, Vanga PR, Ashok M, Giridharan NV (2016) Enhanced photocatalytic activity of hydrothermally grown BiFeO₃ nanostructures and role of catalyst recyclability in photocatalysis based on magnetic framework. App. Phys A 122:1–14

Fan H, Jiang T, Li H, Wang D, Wang L, Zhai J, Xie T (2012) Effect of BiVO₄ crystalline phases on the photoinduced carriers behavior and photocatalytic activity. J Phys Chem C 116:2425–2430

Fischer P, Polomska M, Sosnowska I, Szymanski M (1980) Temperature dependence of the crystal and magnetic structures of BiFeO₃. J Phy C: Solid State Phy 13(10):1931–1940. https://doi.org/10.1088/0022-3719/13/10/012

Gabbasova ZV, Kuz'min MD, Zvezdin AK, Dubenko IS, Murashov VA, Rakov DN, Krynetsky IB (1991) Bi₁₋ₓRₓFeO₃ (R= rare earth): a family of novel magnetoelectrics. Phys Lett A 158(9):491–498. https://doi.org/10.1016/0375-9601(91)90467-M

Gao F, Chen XY, Yin KB, Dong S, Ren ZF, Yuan F, Liu JM (2007) Visible-light photocatalytic properties of weak magnetic BiFeO₃ nanoparticles. Adv Mat 19(19):2889–2892. https://doi.org/10.1002/adma.200602377

Gao T, Chen Z, Zhu Y, Niu F, Huang Q, Qin L, Sun X, Huang Y (2014) Synthesis of BiFeO₃ nanoparticles for the visible-light induced photocatalytic property. Mat Res Bull 59:6–12. https://doi.org/10.1016/j.materresbull.2014.06.022

García-Montaño J, Torrades FA, Pérez-Estrada L, Oller I, Malato S, Maldonado MI, Peral J (2008) Degradation pathways of the commercial reactive azo dye Procion Red H-E7B under solar-assisted photo-Fenton reaction. Environ Sci Technol 42(17):6663–6670. https://doi.org/10.1021/es800536d

Garg A, Sangal VK, Bajpai PK (2016) Decolorization and degradation of Reactive Black 5 dye by photocatalysis: modeling optimization and kinetic study. Des Water Treat 57(38):18003–18015. https://doi.org/10.1080/19443994.2015.1086697

Ghayeni SS, Beatson PJ, Schneider RP, Fane AG (1998) Water reclamation from municipal wastewater using combined microfiltration-reverse osmosis (ME-RO) preliminary performance data and microbiological aspects of system operation. Desalination 116(1):65–80. https://doi.org/10.1016/S0011-9164(98)00058-7

Hadjltaief HB, Galvez ME, Zina MB, Da Costa P (2014) TiO₂/clay as a heterogeneous catalyst in photocatalytic/photochemical oxidation of anionic reactive blue 19. Arab Chem

Hauser AJ, Zhang J, Mier L, Ricciardo RA, Woodward PM, Gustafson TL, Yang FY (2008) Characterization of electronic structure and defect states of thin epitaxial BiFeO₃ films by UV-visible absorption and cathode luminescence spectroscopies. Appl Phys Lett 92(22):222901. https://doi.org/10.1063/1.2939101

Ju MG, Wang X, Liang W, Zhao Y, Li C (2014) Tuning the energy bandgap of crystalline gallium oxide to enhance photocatalytic water splitting: mixed-phase junctions. J Mater Chem A 2(40):17005–17014. https://doi.org/10.1039/C4TA03193H

Ju S, Cai TY (2009) First-principles studies of the effect of oxygen vacancies on the electronic structure and linear optical response of multiferroic BiFeO₃. Appl Phys Lett 95(23):231906. https://doi.org/10.1063/1.3272107

Ke H, Wang W, Wang Y, Xu J, Jia D, Lu Z, Zhou Y (2011) Factors controlling pure-phase multiferroic BiFeO₃ powders synthesized by chemical co-precipitation. J Alloys Comp 509(5):2192–2197. https://doi.org/10.1016/j.jallcom.2010.09.213

Khanna A, Shetty VK (2013) Solar photocatalysis for treatment of Acid Yellow-17 (AY-17) dye contaminated water using Ag@ TiO₂ core-shell structured nanoparticles. Environ Sci Pollu Res 20(8):5692–5707. https://doi.org/10.1007/s11356-013-1582-4

Khanna A, Shetty VK (2014) Solar light induced photocatalytic degradation of Reactive Blue 220 (RB-220) dye with highly efficient Ag@TiO₂ core–shell nanoparticles: a comparison with UV photocatalysis. Solar Ener 99:67–76. https://doi.org/10.1016/j.solener.2013.10.032

Konecoglu G, Safak T, Kalpakli Y, Akgun M (2015) Photocatalytic degradation of textile dye CI Basic Yellow 28 wastewater by Degussa P-25 based TiO₂. Adv Environ Res 4(1):25–38. https://doi.org/10.12989/aer.2015.4.1.025

Li G, Gray KA (2007) The solid–solid interface: explaining the high and unique photocatalytic reactivity of TiO₂-based nanocomposite materials. J Chem Phys 339:173–187

Li S, Lin YH, Zhang BP, Nan CW, Wang Y (2009) Photocatalytic and magnetic behaviors observed in nanostructured BiFeO₃ particles. J App Phy 105:056105. https://doi.org/10.1063/1.3080131

Lin SH, Chen ML (1997) Treatment of textile wastewater by chemical methods for reuse. Water Res 31(4):868–876. https://doi.org/10.1016/S0043-1354(96)00318-1

Liu Y, Zuo R (2013) Morphology and optical absorption of Bi₂Fe₄O₉ crystals via mineralizer-assisted hydrothermal synthesis. Particuology 11(5):581–587. https://doi.org/10.1016/j.partic.2012.11.002

Liu Z, Qi Y, Lu C (2010) High efficient ultraviolet photocatalytic activity of BiFeO₃ nanoparticles synthesized by a chemical co-precipitation process. J Mat Sci: Mat Elec 21:380–384

Markad GB, Kapoor S, Haram SK, Thakur P (2017) Metal free carbon-TiO₂ based composites for the visible light photocatalysis. Sol Energy 144:127–133. https://doi.org/10.1016/j.solener.2016.12.025

Matthews R (1987) Photooxidation of organic impurities in water using thin films of titanium dioxide. J Phys Chem 91(12):3328–3333. https://doi.org/10.1021/j100296a044

Mocherla PS, Karthik C, Ubic R, Ramachandra Rao MS, Sudakar C (2013) Tunable bandgap in BiFeO₃ nanoparticles: the role of microstrain and oxygen defects. Appl Phys Lett 103(2):022910. https://doi.org/10.1063/1.4813539

Muneeswaran M, Jegatheesan P, Giridharan NV (2013) Synthesis of nanosized BiFeO₃ powders by co-precipitation method. J Exper Nanosci 8(3):341–346. https://doi.org/10.1080/17458080.2012.685954

Naumczyk J, Szpyrkowicz L, Zilio-Grandi F (1996) Electrochemical treatment of textile wastewater. Water Sci Tech 34:17–24

Nezamzadeh-Ejhieh A, Karimi-Shamsabadi M (2013) Decolorization of a binary azo dyes mixture using CuO incorporated nanozeolite-X as a heterogeneous catalyst and solar irradiation. Chem engi J 228:631–641. https://doi.org/10.1016/j.cej.2013.05.035

O'neill C, Hawkes FR, Hawkes DL, Esteves S, Wilcox SJ (2000) Anaerobic–aerobic biotreatment of simulated textile effluent containing varied ratios of starch and azo dye. Water Res 34(8):2355–2361. https://doi.org/10.1016/S0043-1354(99)00395-4

Ohno T, Sarukawa K, Matsumura M (2001) Photocatalytic activities of pure rutile particles isolated from TiO2 powder by dissolving the anatase component in HF solution. J Phys Chem B 105:2417–2420

Pala A, Tokat E (2002) Color removal from cotton textile industry wastewater in an activated sludge system with various additives. Water Res 36(11):2920–2925. https://doi.org/10.1016/S0043-1354(01)00529-2

Pan J, Liu G, Lu GQM, Cheng HM (2011) On the true photoreactivity order of {001}, {010}, and {101} facets of anatase TiO₂ crystals.

Angew Chem 50(9):2133–2137. https://doi.org/10.1002/anie.201006057

Ramírez-Aparicio J, Samaniego-Benítez JE, Ramírez-Bon R (2016) TiO$_2$-chabazite semiconductor composites for photocatalytic degradation of rhodamine under sunlight irradiation. Solar Ener 139:258–265. https://doi.org/10.1016/j.solener.2016.09.050

Ruan QJ, Zhang WD (2009) Tunable morphology of Bi$_2$Fe$_4$O$_9$ crystals for photocatalytic oxidation. J Phys Chem C 113(10):4168–4173. https://doi.org/10.1021/jp810098f

Sattler K (2002) The energy gap of clusters, nanoparticles, and quantum dots. Hand book of thin film materials 5:61–97

Shami MY, Awan MS, Anis-ur-Rehman M (2011) Phase pure synthesis of BiFeO$_3$ nanopowders using diverse precursor via co-precipitation method. J Alloys Comp 509(41):10139–10144. https://doi.org/10.1016/j.jallcom.2011.08.063

Simões AZ, Stojanovic BD, Ramirez MA, Cavalheiro AA, Longo E, Varela JA (2008) Lanthanum-doped Bi$_4$Ti$_3$O$_{12}$ prepared by the soft chemical method: Rietveld analysis and piezoelectric properties. Cera Intern 34(2):257–261. https://doi.org/10.1016/j.ceramint.2006.09.019

Smith AM, Mohs AM, Nie S (2009) Tuning the optical and electronic properties of colloidal nanocrystals by lattice strain. Nat Nanotechnol 4(1):56–63. https://doi.org/10.1038/nnano.2008.360

Soltani T, Entezari MH (2013) Photolysis and photocatalysis of methylene blue by ferrite bismuth nanoparticles under sunlight irradiation. J Mol Cat A: Chem 377:197–203. https://doi.org/10.1016/j.molcata.2013.05.004

Tan T, Xie W, Zhu G, Shan J, Xu P, Li L, Wang J (2015) Fabrication and photocatalysis of BiFeO$_3$ with inverse opal structure. J Porous Mat 22(3):659–663. https://doi.org/10.1007/s10934-015-9938-4

Vinu R, Madras G (2012) Environmental remediation by photocatalysis. J Indian Institute Sci 90:189–230

Wang X, Lin Y, Ding X, Jiang J (2011a) Enhanced visible-light-response photocatalytic activity of bismuth ferrite nanoparticles. J Alloys Compd 509(23):6585–6588. https://doi.org/10.1016/j.jallcom.2011.03.074

Wang X, Lin Y, Zhang ZC, Bian JY (2011b) Photocatalytic activities of multiferroic bismuth ferrite nanoparticles prepared by glycol-based sol–gel process. J Sol-Gel Sci Technol 60(1):1–5. https://doi.org/10.1007/s10971-011-2542-4

Wang X, Mao W, Wang Q, Zhu Y, Min Y, Zhang J, Huang W (2017) Low-temperature fabrication of Bi$_{25}$FeO$_{40}$/rGO nanocomposites with efficient photocatalytic performance under visible light irradiation. RSC Adv 7:10064–10069

Wang X, Zhu J, Jiang J, Wei S (2010) One-pot synthesis and optical properties of monodisperse ZnSe colloidal microspheres. Appl Phys A Mater Sci Process 99(3):651–656. https://doi.org/10.1007/s00339-010-5692-2

Wang Y, Xu G, Yang L, Ren Z, Wei X, Weng W, Du P, Shen G, Han G (2009) Hydrothermal synthesis of single-crystal bismuth ferrite nanoflakes assisted by potassium nitrate. Ceram Int 35(3):1285–1287. https://doi.org/10.1016/j.ceramint.2008.04.016

Xia Y, Yin L (2013) Core–shell structured α-Fe$_2$O$_3$@TiO$_2$ nanocomposites with improved photocatalytic activity in the visible light region. Phys Chem Chem Phys 15(42):18627–18634. https://doi.org/10.1039/c3cp53178c

Xian T, Yang H, Dai J, Wei Z, Ma J, Feng W (2011) Preparation and photocatalytic performance of nano-bismuth ferrite with tunable size. Chinese J Catal 32(4):618–623

Xie H, Wang K, Jiang Y, Zhao Y, Wang X (2014) An improved co-precipitation method to synthesize three bismuth ferrites. Synthesis Reactivity Inorganic Metal-Org nano-Met Chem 44(9):1363–1367. https://doi.org/10.1080/15533174.2013.801859

Yang X, Wang X, Zhang Z (2005) Synthesis and optical properties of single-crystalline bismuth selenide nanorods via a convenient route. J Cryst Growth 276:566–570

Zalesskii AV, Frolov AA, Khimich TA, Bush AA (2003) Composition-induced transition of spin-modulated structure into a uniform anti-ferromagnetic state in a Bi$_{1-x}$la$_x$FeO$_3$ system studied using 57 Fe NMR. Physics-Solid State 45(1):141–145. https://doi.org/10.1134/1.1537425

Zhang L, Zhang X, Zou Y, Xu YH, Pan CL, Hu JS, Hou CM (2015) Hydrothermal synthesis, influencing factors and excellent photocatalytic performance of novel nanoparticle-assembled Bi$_{25}$FeO$_{40}$ tetrahedrons. Cryst Eng Comm 17(34):6527–6537. https://doi.org/10.1039/C5CE00743G

Zhang L, Zou Y, Song J, Pan CL, Sheng SD, Hou CM (2016) Enhanced photocatalytic activity of Bi$_{25}$FeO$_{40}$–Bi$_2$WO$_6$ heterostructures based on the rational design of the heterojunction interface. RSC Advs 6(31):26038–26044. https://doi.org/10.1039/C6RA00334F